Volume 13 | Number 1 | 6 January 2026

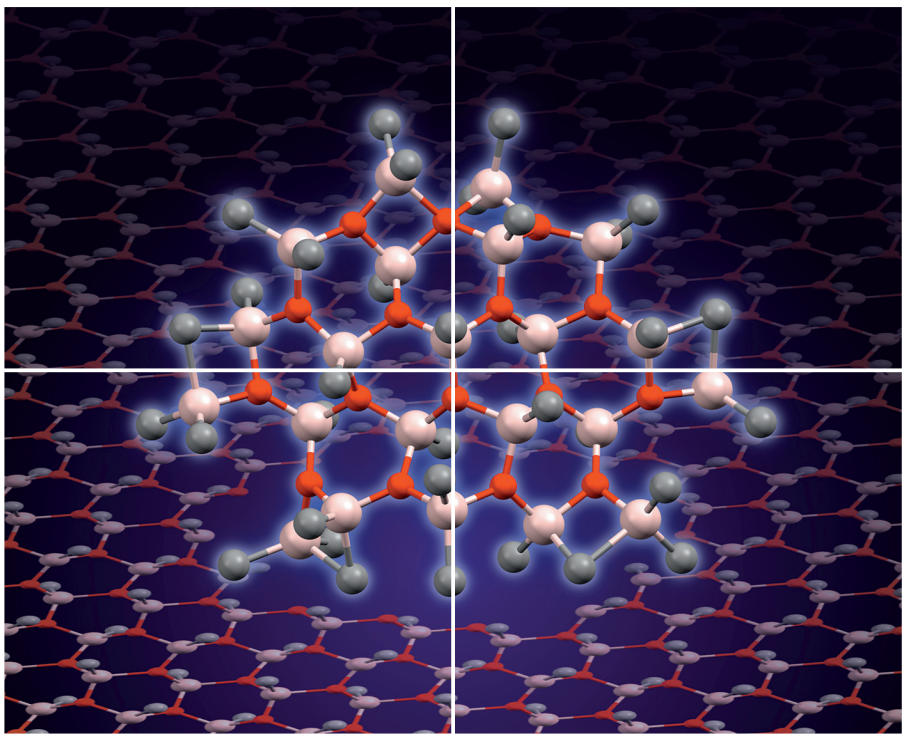

INORGANIC CHEMISTRY

FRONTIERS

CCS 中国化学会 CHINESE CHEMICAL SOCIETY

PEKING UNIVERSITY 1898

ROYAL SOCIETY OF CHEMISTRY

rsc.li/frontiers-inorganic

INORGANIC CHEMISTRY
FRONTIERS

RESEARCH ARTICLE

View Article Online
View Journal | View Issue

Cite this: *Inorg. Chem. Front.*, 2026, **13**, 20

Structure of the most stable methylaluminoxane anion $[(MeAlO)_{16}(Me_3Al)_6Me]^-$ and its precursor

Munmun Bharti, Aleksi Vähäkangas, Perttu Hanhisalo, Scott Collins and Mikko Linnolahti *

Methylaluminoxane (MAO) serves as the predominant cocatalyst in olefin polymerization, yet the structure of its dominant anionic component observed in mass spectrometry has remained problematic despite the recent breakthrough crystallographic characterization of an MAO component reported (L. Luo *et al.*, *Science*, 2024, **384**, 1424–1428), which revealed sheet-like rather than cage-like structures. Here, we resolve this long-standing puzzle by introducing new structural models using hydrocarbon–aluminoxane structural analogy rather than traditional hydrolysis approaches. By extracting finite molecular segments from optimized infinite sheets using an ovalene-like framework, we identified neutral precursor structures that form the dominant MAO anion through $[Me_2Al]^+$ abstraction. Our highest-level *ab initio* calculations reveal that the optimal structure produces an anionic species over 50 kJ mol^{-1} more stable than previously reported models. Critically, our model exhibits notable structural similarities with the crystallographically characterized structure. These findings resolve the theory–experiment discrepancy and provide accurate structural foundations for understanding MAO activation mechanisms in industrial catalysis.

Received 24th September 2025,
Accepted 19th November 2025

DOI: 10.1039/d5qi01957e

rsc.li/frontiers-inorganic

Introduction

Methylaluminoxane (MAO) has been an indispensable cocatalyst in olefin polymerization since its discovery in the late 1970s.[1,2] Despite its extensive usage in industrial and laboratory settings for activating metallocene catalysts,[3,4] the precise structure of MAO has remained elusive for decades.[5] This structural ambiguity persists primarily due to the complex oligomeric nature of MAO, which exists as an equilibrating mixture of various $(MeAlO)_n(Me_3Al)_m$ oligomers.[6] Despite this complexity, improvements to MAO include methods for reducing trimethylaluminum content,[7,8] improving stability towards gelation[9,10] and most importantly increasing its activator content.[11] Though other activators are available,[12–14] MAO remains the dominant choice for commercial use, particularly in supported form.[15]

Over the years, computational studies have proposed several structural motifs for MAO components, including cage, chain, ring, nanotube and sheet structures.[16–18] Recent computational investigations have increasingly suggested the thermodynamic preference of sheet structures composed of fused six-membered $(MeAlO)_n$ rings with edges saturated by associated trimethylaluminum (TMA).[18,19]

The recent crystallographic characterization of a component of MAO, identified as $(MeAlO)_{26}(Me_3Al)_9$ (hereinafter 26,9) sheet structure confirmed these findings.[20] The isolated material was superior to commercial MAO when compared at the same Al : Zr ratio for metallocene-catalyzed olefin copolymerization. Based on the X-ray structure and DFT study of reactions between 26,9 and 1–2 equivalents of tetrahydrofuran (THF), a catalyst activation mechanism *via* $[Me_2Al]^+$ abstraction[11,21] was proposed. No experimental details were provided regarding catalyst activation or ion-pair formation. More recently, total X-ray scattering characterization of commercial MAO using synchrotron radiation indicated that most of the material was sheet-like rather than cage-like.[22] Moreover, sheet-sheet aggregation was also evident in these X-ray scattering experiments. Most recently, high-field, solid-state ^{27}Al NMR studies have clarified the abundance and main types of Al sites present in MMAO.[23] Sites responsible for $[Me]^-$ abstraction from Cp_2ZrMe_2 or adduct formation with Cp_2ZrMe_2 or Lewis base donors (THF) were identified. Their local structure was confirmed by DFT calculation of chemical shift tensors and quadrupolar coupling constants. Bridging Al–Me–Al groups,[24] as found in $O_2Al(Me)$-μ-Me-$AlMe_2O$ moieties and reactive towards Lewis bases,[25] are important for either adduct formation or methide abstraction. These types of sites are found in all structural models proposed for MAO containing Me_3Al, though they are especially abundant along the edges of sheet structures.

The reactions of metallocene and Lewis base donors, such as THF and phosphines, with MAO have been extensively

Department of Chemistry and Sustainable Technology, University of Eastern Finland, Joensuu Campus, Yliopistokatu 7, FI-80100 Joensuu, Finland.
E-mail: mikko.linnolahti@uef.fi

studied using various spectroscopic methods including NMR.[3–5,11] These studies were primarily aimed at identifying the cationic portion of any outer-sphere ion pairs formed. In the case of hard Lewis bases, cations of the type $[Me_2Al(D)_2]^+$ (D = 2e donor) are formed.[5,11] ESI-MS studies of these reactions were initiated about a decade ago[26] and the outer-sphere cations detected from reaction of Lewis bases[27] or metallocene complexes[28] with MAO were entirely consistent with these earlier studies indicating a strong correlation between ESI-MS results and solution spectroscopic techniques.

Regardless of the additive in use, the negative ion mass spectra of hydrolytic MAO (W.R. Grace) in the presence of metallocene and other donors were dominated by an anion with *m*/*z* 1375.[27,28] Based on MS-MS studies of its collision-induced fragmentation, the likely composition of the anion has been determined as $[(MeAlO)_{16}(Me_3Al)_6Me]^-$ (hereafter $[16,6]^-$).[29] At higher additive levels, particularly when using the chelating donor $(Me_3SiO)_2SiMe_2$ (OMTS), the intensity of higher *m*/*z* anions increased.[29] However, when OMTS exceeded the Me_3Al content of the MAO in use, lower *m*/*z* ions were seen (*e.g.* see Fig. 8). These high OMTS concentrations caused degradation of the MAO, as was known from earlier studies involving similar donors and cryoscopy.[30] Surprisingly, the $[26,8]^-$ anion, which might have formed from the isolated 26,9 sheet and OMTS, was a minor component of these mixtures under all conditions.

The mechanism of MAO formation by hydrolysis of Me_3Al has been studied using *ab initio* methods.[31,32] A systematic study of Me_3Al hydrolysis was conducted for MAO ($(MeAlO)_n(Me_3Al)_m$) up to $n = 8$ and $m = 5$ at the MP2 level of theory.[33] A directed search of stepwise hydrolysis reactions based on electronic energy and DFT was used to locate higher molecular weight (MW) components for $n \leq 18$ and $m \leq 7$.[34] The final study, based on the Gibbs free energy of formation through hydrolysis, established that in this size range, 16,6 was the most stable neutral sheet.[19] Given this finding, it was natural to investigate the reactivity of this model sheet towards ion-pair formation. In comparing both activation mechanisms,[35] the 16,6 sheet was more reactive to $[Me]^-$ abstraction involving Me_3Al-OMTS as a methyl donor. According to the most recent systematic study,[36] the 16,6 sheet formed less stable $[Me_2Al(OMTS)][n,m]$ ion-pairs than those formed from other sheets, especially the 26,9 sheet. However, the ESI-MS experiments[29] contradicted these results as the intensity of the $[16,6]^-$ anion was greater than any other anion detected (*vide infra*).

These inconsistencies between the lowest energy 16,6 neutral and experimental *versus* theoretical observations encouraged us to revisit the $[16,6]^-$ anion structure and its precursor. We suspected that the previously identified 16,6 sheet might not correspond to the material produced through the hydrolysis of Me_3Al and subsequent oligomerization of low MW MAO.[37]

In this work, we introduce new sheet models 16,7 as possible precursors to the dominant $[16,6]^-$ anion, employing hydrocarbon–aluminoxane structural analogy rather than TMA hydrolysis studies. The structural analogy between aluminoxanes and hydrocarbons has been established as a powerful framework for understanding structural preferences in aluminoxane.[38–40] Despite differences in electronic properties due to polar Al–O *versus* nonpolar C–C bonds, aluminoxanes can form structural motifs analogous to their hydrocarbon counterparts.[39,40] Of particular relevance is the analogy to graphane[41] (fully hydrogenated graphene), where hydrogen atoms adopt alternating up-down positions to minimize steric repulsions. This principle of alternating substituent arrangements to reduce steric interactions extends to other hydrocarbon systems, including hydrogenated fullerenes,[38] where 'in-out' isomerism enhances structural stability.

Our computational studies demonstrate that these new 16,7 sheets have comparable stability to the original 16,6 neutral sheet. Additionally, anions formed from these precursors *via* $[Me_2Al]^+$ abstraction are much more stable than the previously published $[16,6]^-$ anion. We also studied $[Me_2Al(OMTS)][16,6]$ ion-pair stabilities to relate these findings more directly to experiments.

Results and discussion

From infinite sheets to finite molecular models

Building on the established hydrocarbon–aluminoxane analogy, we systematically investigated the methyl group arrangements in infinite MAO $(MeAlO)_\infty$ sheets to identify the energetically preferred arrangement. The $(MeAlO)_\infty$ sheet consists of fused six-membered rings with methyl groups projecting only from aluminum atoms, resulting in half the number of substituents as hydrocarbon analogues. Despite this difference, the fundamental principle of minimizing steric interactions through substituent orientation remains applicable.

To enable a comprehensive yet computationally tractable analysis, we selected $(MeAlO)_8$ as our representative unit cell. Smaller than 8 units would inadequately capture the range of possible methyl configurations, while larger cells would introduce unnecessary complexity.

We focused exclusively on balanced methyl distributions (four up, four down), as unequal distributions would create asymmetric strain, favoring curved structures (like cages or nanotubes) over extended sheets. Our computational screening of all possible balanced arrangements within the $(MeAlO)_8$ unit cell revealed that the dudu_udud arrangement exhibited the lowest electronic energy (Fig. 1). In this arrangement, methyl groups alternate directions within each row (down–up–down–up and up–down–up-down), representing the closest approximation to perfect alternation possible in aluminoxane systems. Unlike hydrocarbon counterparts, where strictly alternating arrangements are feasible, the structural constraint of three methyl groups per six-membered ring in MAO prevents complete alternation. Nevertheless, this dudu_udud pattern effectively minimizes steric interactions and establishes a foundation for constructing finite molecular models.

Having established the optimal methyl arrangement in infinite sheets, we applied these insights to target the dominant

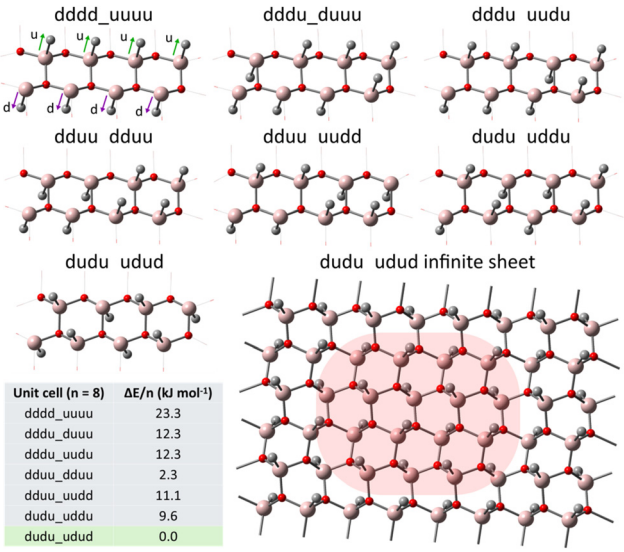

Unit cell (n = 8)	ΔE/n (kJ mol^{-1})
dddd_uuuu	23.3
dddu_duuu	12.3
dddu_uudu	12.3
dduu_dduu	2.3
dduu_uudd	11.1
dudu_uddu	9.6
dudu_udud	0.0

Fig. 1 $(MeAlO)_8$ unit cells (unoptimized structures (except dudu_udud infinite sheet) only for clear visualization of methyl arrangement. Optimized structures are in SI.) showing different methyl group arrangements for $(MeAlO)_\infty$ sheets and their relative electronic energies per MeAlO unit (kJ mol^{-1}) at M06-2X level. The most stable infinite sheet formed from the most stable unit cell with a representative cut, highlighted with pink, giving an ovalene-like structure for n = 16. Hydrogens omitted for clarity. .

$[16,6]^-$ anion observed in ESI-MS experiments. We constructed finite molecular models by extracting segments from the lowest-energy infinite sheet and saturating the edges with TMA. For this purpose, ovalene – a polycyclic aromatic hydrocarbon containing 32 carbon atoms in fused six-membered rings – provides an ideal topological framework. When adapted to aluminoxane chemistry, this ovalene-like structure yields a 16,7 neutral composition that can form $[16,6]^-$ anion through $[Me_2Al]^+$ abstraction. We systematically extracted all unique ovalene-like structural isomers from the infinite sheet, saturated their edges with TMA, and optimized the resulting structures at the M06-2X/TZVP level. This analysis identified two energetically preferred isomers, β and γ (Fig. 2). These isomers preserve essential features of the alternating methyl pattern while adapting to the constraints of finite molecular structure and edge-saturating TMA groups.

These initial isomers (β and γ) offered valuable insights, but we recognized that finite molecular systems might not exhibit the same structural preferences as the infinite sheets. Two factors distinguish the finite 16,7 structure from the periodic system: first, its 9 methyl groups in O_3AlMe environments (corresponding to the sheet framework) create an inherently unbalanced distribution (4 up, 5 down), preventing the optimal symmetric arrangement identified for infinite sheets; second, TMA-saturated edges introduce structural constraints and interactions absent in the periodic models. Given the differences, we screened the down-up combinations in the ovalene-like framework, locating an isomer (α, Fig. 2) with significantly lower energy than both β and γ, confirming that structural principles from infinite sheets require adaptation for finite molecular systems. We used Greek letters α, β, and γ to name these 16,7 structural isomers in increasing order of energy, starting with α as the lowest-energy isomer.

Beyond methyl group arrangements within the sheet framework, these molecular systems exhibit configurational flexibility at edge sites. The Me_2AlO groups at these positions can adopt different configurational states with minimal energy barriers (Fig. 3). Specifically, Me_2AlO can bond either with a bridging AlMe group (with 3-coordinate oxygen (3-C O)) or with oxygen (creating 4-coordinate oxygen (4-C O)). This bonding flexibility generates four distinct configurational isomers for each 16,7 isomer: O3 (both edge sites 3-coordinate), O4a (left site 3-coordinate, right site 4-coordinate), O4b (left site 4-coordinate, right site 3-coordinate), and 2O4 (both sites 4-coordinate). This configurational diversity significantly impacts overall structural stability and must be considered when identifying optimal 16,7 structures.

Energetic analysis

Accurate assessment of these configurations required addressing a significant methodological challenge. Our recent studies demonstrated that the M06-2X functional, widely used for MAO systems due to its demonstrated accuracy for Al–C (bridging) interactions, systematically overestimates the stability of 4-C O structures.[36]

This represents a methodological artifact rather than true energetic preferences. Higher-level calculations (MP2, CCSD (T)) consistently show that 3-C O configurations are thermodynamically favored, creating a problematic discrepancy when comparing (O3, O4a, O4b, and 2O4) configurations. To overcome this limitation, we performed RI-MP2/def2-TZVP single-point energy calculations on the M06-2X/TZVP optimized geometries, providing more accurate energetics while maintaining computational feasibility for these large molecular systems. These RI-MP2 energies were used to correct the free energies obtained at the DFT level, enabling a reliable comparison of configurational isomers.

We next analyzed the relative energetics of our candidate 16,7 structures using the previously reported 16,6 neutral and corresponding $[16,6]^-$ (ref. 19) anion as references (Table 1). While the neutral compositions differ (16,6 *vs.* 16,7), both can form $[16,6]^-$ anions through different pathways: $[Me]^-$ abstraction to 16,6 *versus* $[Me_2Al]^+$ abstraction from 16,7. The neutral species can be directly compared through the TMA dissociation relationship 16,7 → 16,6 + $\frac{1}{2}Al_2Me_6$. This comparison is entirely equivalent to another metric of thermodynamic stability, the free energy of hydrolysis of Al_2Me_6,[27] in this case at constant n.

For the three structural isomers (α, β, and γ), we performed a thorough energetic analysis across all edge configurations. The results dramatically illustrate the limitations of M06-2X discussed earlier: while M06-2X predicts 4-C O configurations (O4a, O4b, and 2O4) as more stable, RI-MP2 corrections systematically reverse this ordering, favoring 3-C O (O3) configurations. Systematic differences in vibrational entropy further strengthen this preference – 3-C O configurations consistently

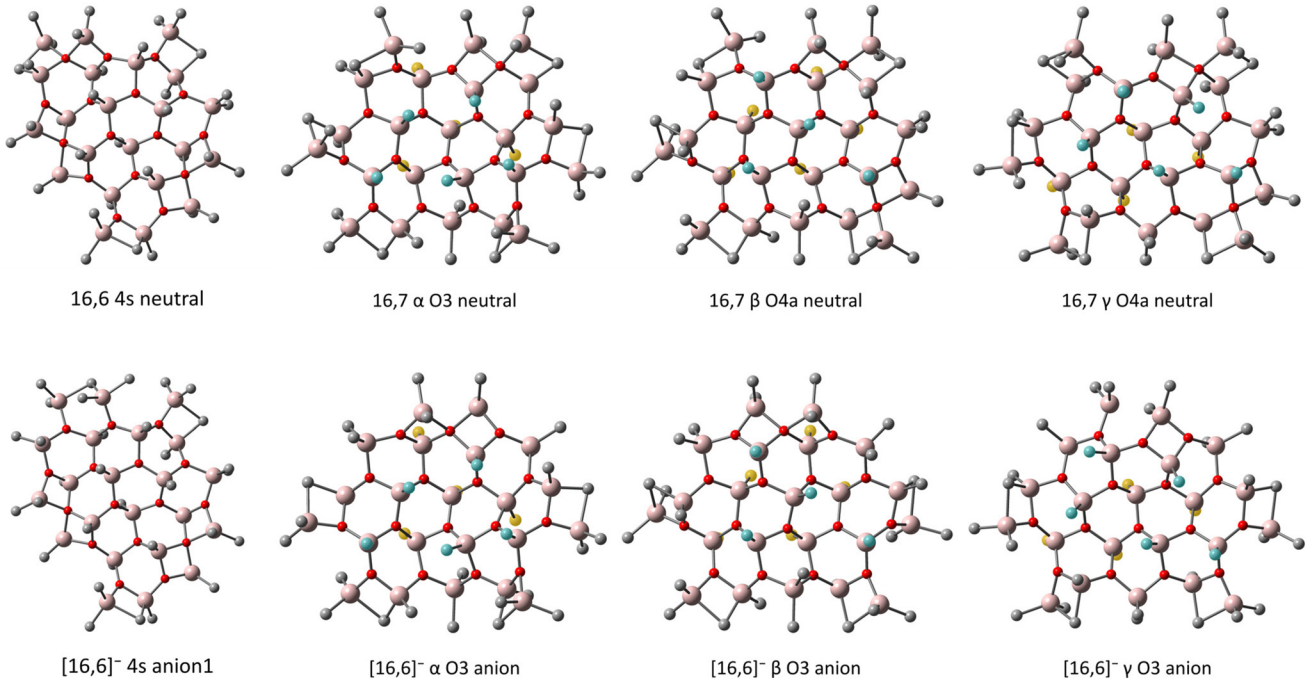

Fig. 2 Lowest energy configurations of ovalene-like 16,7 neutrals and $[16,6]^-$ anions compared to the lowest energy 16,6 neutral[19] and the corresponding $[16,6]^-$ anion. Blue and yellow atoms show Me groups facing up and down, respectively, illustrating the differences between α, β, and γ isomers. Hydrogens are omitted for clarity.

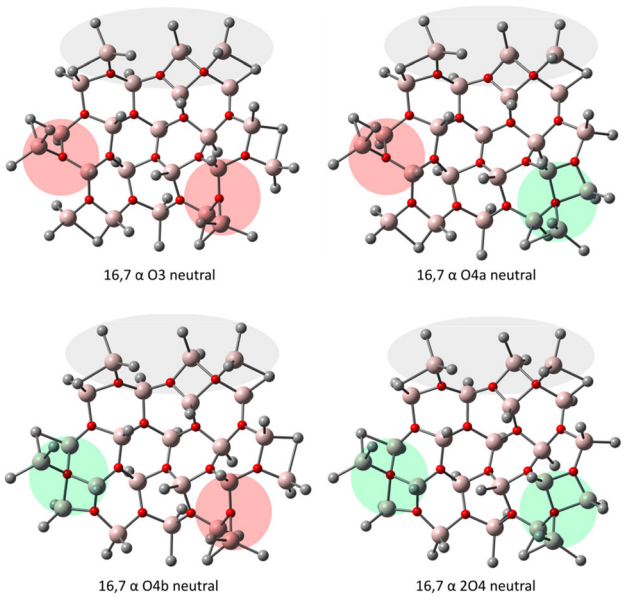

Fig. 3 Configurations of ovalene-like 16,7. Grey area represents the reactive site, pink area represents the 3-C O sites, and green area represents the 4-C O sites.

show higher entropy than their 4-C counterparts, providing additional thermodynamic stabilization for configurations with 3-C O at the higher level of theory.

The two isomers derived from the periodic calculations (β and γ) showed promising electronic energies, with their most stable configurations lying approximately 30 kJ mol^{-1} below the reference 16,6 neutral at both DFT and RI-MP2 levels. However, these structures became less competitive when entropic contributions were included to compute free energies (ΔG).

At our highest theoretical-level (RI-MP2-corrected energies in fluorobenzene), the α structure outperformed β and γ by 10–15 kJ mol^{-1} in electronic energy and 15–20 kJ mol^{-1} in free energy. Most significantly, the α 16,7 neutral achieves comparable stability to the previously reported 16,6 reference structure. This finding validates our approach of adapting infinite sheet principles to finite molecular constraints and identifying a thermodynamically competitive alternative.

Anion formation

Having established the relative stabilities of neutral 16,7 structures, we investigated their ionization to form $[16,6]^-$. We focus on the $[Me_2Al]^+$ abstraction pathway (anionization), which directly connects our stable 16,7 structures to the experimentally dominant $[16,6]^-$ species. In our previous work,[36] calculations on analogous MAO sheet structures demonstrate that $[Me_2Al]^+$ abstraction from MAO sheets is kinetically facile using OMTS as the donor. Table 2 provides the energy changes for this process involving OMTS as the common donor in gas phase or fluorobenzene (entries 1–12). For comparison we also provide the results for the isolated 26,9 sheet (entry 13). Finally, the energy change for the methide abstraction process involving the original 16,6 sheet is also given (entry 14). We also studied formation of the corresponding outer-sphere ion-pairs $[Me_2Al(OMTS)][16,6]$ for two of these anions and will discuss those later.

Table 1 Energetics of the new 16,7 neutrals and their corresponding $[16,6]^-$ anions relative to previously published 16,6 neutral and the corresponding $[16,6]^-$ anion. All values are in kJ mol^{-1}

	M06-2X/def2-TZVP				RI-MP2	RI-MP2 energy corrected		
	ΔE	ΔG-qh[a]	ΔE (PhF)	ΔG-qh-tr[b] (PhF)	ΔE (RI-MP2, sp)	ΔG-qh[a]	ΔE (PhF)	ΔG-qh-tr[b] (PhF)
Neutral sheets								
16,6 4s + (1/2 Al_2Me_6)	0.0	0.0	0.0	0.0	0.0	0.0	0.0	0.0
16,7 α O3	−13.0	20.7	−13.7	10.5	−23.8	9.9	−24.5	−0.3
16,7 α O4a	−47.3	−0.7	−44.3	−3.6	−42.0	4.5	−39.0	1.6
16,7 α O4b	−12.4	32.6	−18.7	20.6	−8.6	36.4	−14.9	24.4
16,7 α 2O4	−48.4	8.5	−48.8	1.7	−27.5	29.4	−27.9	22.7
16,7 β O3	1.5	38.8	2.9	37.4	−9.1	28.2	−7.7	26.9
16,7 β O4a	−32.6	21.0	−30.0	15.4	−27.0	26.6	−24.4	21.0
16,7 β O4b	2.9	57.2	0.8	45.5	8.3	62.6	6.2	50.9
16,7 β 2O4	−35.3	29.7	−32.8	23.5	−12.3	52.7	−9.8	46.6
16,7 γ O3	−0.5	32.9	−3.3	26.2	−12.4	21.1	−15.1	14.3
16,7 γ O4a	−30.1	10.5	−27.2	5.6	−29.5	11.2	−26.6	6.2
16,7 γ O4b	−16.4	30.2	−18.3	21.9	−11.5	35.0	−13.5	26.7
16,7 γ 2O4	−40.2	20.1	−37.9	14.7	−21.1	39.2	−18.8	33.8
Anions								
$[16,6]^-$ 4s anion1	0.0	0.0	0.0	0.0	0.0	0.0	0.0	0.0
$[16,6]^-$ 4s anion2	9.5	8.1	10.3	7.4	9.9	8.5	10.8	7.8
$[16,6]^-$ α O3	−28.1	−42.3	−26.2	−40.1	−39.7	−53.9	−37.9	−51.7
$[16,6]^-$ α O4a	−35.7	−35.0	−37.3	−39.0	−29.1	−28.4	−30.7	−32.3
$[16,6]^-$ α O4b	−40.7	−40.1	−39.9	−38.4	−36.2	−35.6	−35.4	−33.9
$[16,6]^-$ α 2O4	−51.7	−39.4	−52.6	−41.0	−25.8	−13.5	−26.7	−15.0
$[16,6]^-$ β O3	−11.4	−6.6	−8.3	−11.7	−18.1	−13.3	−15.0	−18.4
$[16,6]^-$ β O4a	−21.7	−8.3	−25.1	−16.6	−10.9	2.5	−14.3	−5.8
$[16,6]^-$ β O4b	−22.9	−12.2	−18.8	−10.7	−12.7	−2.0	−8.6	−0.5
$[16,6]^-$ β 2O4	−34.6	−12.9	−38.0	−16.9	−7.9	13.8	−11.3	9.8
$[16,6]^-$ γ O3	8.7	1.8	10.1	5.3	−3.9	−10.9	−2.5	−7.3
$[16,6]^-$ γ O4a	3.0	1.9	3.0	0.3	2.8	1.7	2.8	0.1
$[16,6]^-$ γ O4b	5.0	5.8	3.3	2.7	6.9	7.7	5.2	4.5
$[16,6]^-$ γ 2O4	4.2	11.5	0.1	7.7	22.3	29.6	18.2	25.8

[a] Free energy corrected for low E vibrations using a quasi-harmonic approximation.[42] [b] ΔG-qh corrected for the reduced translational entropy in solution.[43]

Table 2 Ionization energies[a] for the reaction 16,7 + OMTS → $[Me_2Al(OMTS)]^+$ + $[16,6]^-$

Entry	Anion	ΔE	ΔE (MP2)	ΔE (PhF)	ΔG-qh-tr[d] (PhF)	ΔE (PhF) MP2	ΔG-qh-tr[d] (PhF) MP2
1	$[16,6]^-$ α O3	134.3	149.2	−47.3	−52.8	−32.4	−37.9
2	$[16,6]^-$ α O4a	160.9	178.0	−27.9	−37.6	−10.7	−20.4
3	$[16,6]^-$ α O4b	155.9	170.9	−30.5	−37.0	−15.5	−22.0
4	$[16,6]^-$ α 2O4	146.0	166.8	−38.6	−45.0	−17.8	−24.2
5	$[16,6]^-$ β O3	136.5	156.1	−46.0	−51.4	−26.4	−31.8
6	$[16,6]^-$ β O4a	160.3	181.2	−29.9	−34.2	−9.0	−13.3
7	$[16,6]^-$ β O4b	123.5	144.1	−54.4	−58.5	−33.8	−37.9
8	$[16,6]^-$ β 2O4	150.0	169.4	−40.0	−42.7	−20.6	−23.2
9	$[16,6]^-$ γ O3	158.5	173.5	−21.4	−23.1	−6.4	−8.1
10	$[16,6]^-$ γ O4a	182.4	197.4	−4.6	−7.5	10.3	7.4
11	$[16,6]^-$ γ O4b	170.7	183.5	−13.2	−21.4	−0.4	−8.6
12	$[16,6]^-$ γ 2O4	193.7	208.4	3.2	−9.3	17.9	5.5
13[b]	$[26,8]^-$	131.6	147.2	−47.7	−56.6	−32.1	−41.0
14[c]	$[16,6]^-$	176.6	171.5	−3.9	−3.2	−9.0	−8.3

[a] Electronic energies (ΔE) and Gibbs free energies (ΔG) in kJ mol^{-1} at 298 K. [b] For the reaction 26,9 + OMTS → $[Me_2Al(OMTS)]^+$ + $[26,8]^-$. [c] For the reaction 16,6 + OMTS-$AlMe_3$ → $[Me_2Al(OMTS)]^+$ + $[16,6]^-$. [d] The quasi-harmonic free energy including translational entropy corrections.

First, it is clear that both the α, and β 16,7 sheets are more reactive to anionization than the γ sheets. As illustrated in Fig. 4, abstraction from the sheet edge (red circle) triggers a reorganization of Me_2Al groups (grey triangles) that depends critically on the orientations of neighboring methyl groups (green/blue atoms). For stable anion formation, the methyl groups adjacent to the ionization site must point in opposite directions (green shows Me facing down and blue facing up), enabling formation of a stabilizing 4-C O environment. Both the α and β isomers satisfy this constraint, with oppositely oriented methyl groups (one green and one blue) at the critical positions. In contrast, γ has both relevant methyl groups point-

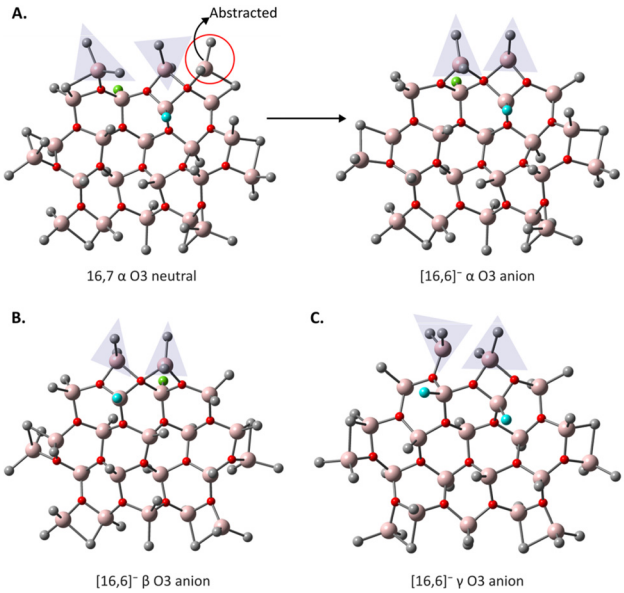

Fig. 4 A. $[Me_2Al]^+$ abstraction mechanism and reorganization of adjacent edge Me_2Al groups (grey triangles) in 16,7 α O3 neutral to form the consequent $[16,6]^-$ anion. B. $[16,6]^-$ anion formed from 16,7 β O3 neutral. C. $[16,6]^-$ anion formed from 16,7 γ O3 neutral. Green and blue atoms represent the methyl groups in opposite directions affecting the reorganization ability of Me_2Al groups (grey triangles).

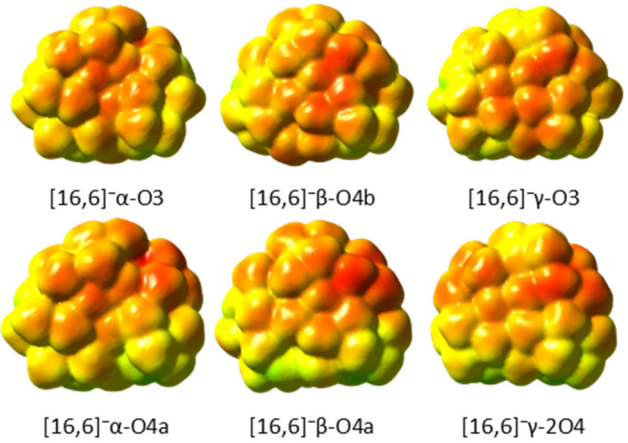

Fig. 5 Electrostatic potential maps of sheet anions corresponding to the most reactive neutral sheet (top) and the least reactive sheet (bottom) of each type. The potential varies between +0.1 (red) and −0.1 (blue) excess charge for each anion.

ing in the same direction (both are blue), preventing the formation of stabilizing 4-C O. Consequently, the γ sheets cannot readily form stable $[16,6]^-$ anions.

The other thing that is striking is that for the α to γ sheets, the reactivity of each individual isomer is quite different when it comes to anion formation. In the case of the α sheet, the O3 isomer is the most reactive neutral, while for the β sheet it is the O4b isomer which has comparable reactivity, even though that neutral is *ca.* 30 kJ mol^{-1} less stable than 16,7 α O3 (Table 1). Finally, in the case of the more stable γ sheets, as they lack the optimal up-down Me arrangement, the O3 and O4b arrangements have lower, but comparable reactivity to each other, and are significantly more reactive than the other two isomers.

These reactivity differences are *uncorrelated* with the stability differences of the corresponding neutrals and even global anion stability (Table 1). To understand this, we obtained electrostatic potential surfaces for these anions. Fig. 5 compares these surfaces for the most (top) and least reactive neutral (bottom) for each type of sheet anion. There is a pronounced difference in charge delocalization that is clearly visible. The least reactive sheets give rise to anions with "hot spots" (red color) and cooler zones (yellow green), while the more reactive sheets afford anions that are more uniform in color. The detailed charge distributions are obviously different for each type of sheet anion. However, the $[16,6]^-$ γ O3 anion features more charge localization than the $[16,6]^-$ α O3 anion, in accord with the significant reactivity difference of the corresponding neutrals.

Concerning isolated $[16,6]^-$ anions, the most striking finding is the exceptional stability of our ovalene-like α structure. According to RI-MP2-corrected calculations in fluorobenzene,[44] the $[16,6]^-$ anion ($[16,6]^-$ α O3) lies 51.7 kJ mol^{-1} below the reference anion in free energy (Table 1). This dramatic stabilization is particularly remarkable given that the neutral precursors (α 16,7 and reference 16,6) show comparable stability. This difference, along with ionization energies for the reaction with OMTS (Table 2), indicates a much greater thermodynamic driving force for anionization in our ovalene-like model, though kinetic factors would also influence actual catalyst activation processes.[35]

Edge configuration preferences also shift dramatically upon ionization. While the neutrals show modest preference for O3 over O4 variants, this selectivity is substantially amplified in the anions. The explanation lies in the structural reorganization during $[Me_2Al]^+$ abstraction. In neutrals, the reactive site experiences steric interactions with nearby non-reactive edges, partially relieved by O4 configurations. Anion formation eliminates this steric strain, allowing full realization of the inherent energetic advantage of the O3 configuration.

These factors – ovalene-like framework, α isomer, and enhanced O3 preference – synergistically produce the most stable $[16,6]^-$ anion reported in the literature.

Understanding vibrational entropy differences

To explain the systematic entropy differences between 3-C O and 4-C O edge configurations, we analyzed the gas-phase structures, vibrational frequencies, and normal modes of neutral 16,7 α and $[16,6]^-$ α anion models.

Our analysis reveals that 4-C O configurations show consistently higher frequencies in low-frequency regions (0–300 cm^{-1}) than their 3-C O counterparts. The frequency differences are 3.6–7.8 cm^{-1} for 16,7 and 4.3–9.7 cm^{-1} for $[16,6]^-$. While modest for individual vibrations, these differences accumulate across roughly 150 normal modes, causing significant entropy

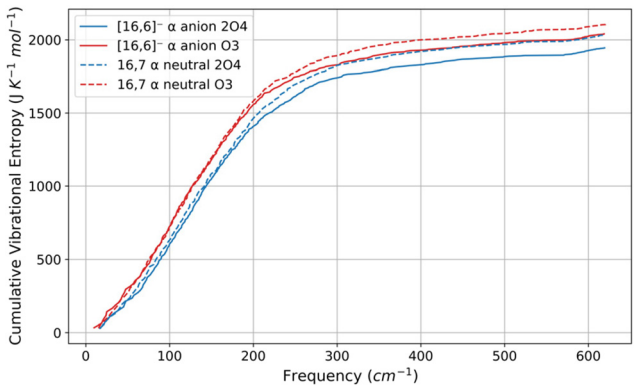

Fig. 6 Cumulative vibrational entropies of [16,6]$^-$ and 16,7 α 2O4 and O3 variants.

differences (Fig. 6). For example, the vibrational entropy of 16,7 α 2O4 is 2181 and 16,7 α O3 is 2256 J K^{-1} mol^{-1}. Vibrational entropy is by far the most significant contributor to the total entropy of these molecules (2556 and 2631 J K^{-1} mol^{-1}, respectively) and other large sheet models.

These vibrational entropy differences are likely caused by structural differences between 3-C O and 4-C O sites. The 3-C O sites have two individual 4-membered rings, while the 4-C O sites have a spirocyclic ring structure (Fig. 3). The spirocyclic ring has fewer degrees of freedom than the two individual rings, lowering entropy[45] in 4-C O configurations. This entropy reduction appears as vibrational entropy because the 3-C O and 4-C O sites are embedded within larger, rigid frameworks that restrict their contribution to the molecule's translational and rotational entropy.

Another interesting feature is that hydrogen atoms of adjacent methyl groups are closer to each other (*ca.* 0.1 Å) near 4-C O sites, restricting available space for motion. This restricted space could lead to steeper potential energy surfaces and higher vibrational frequencies. Greater separation near 3-C O sites would allow more effortless motion, generating lower frequencies and higher entropy. However, we note that such analysis of these hydrogen distances shows no statistical significance.

Configurational ensemble thermodynamics

To quantify the effects of configurational flexibility, we employed ensemble statistical thermodynamics to calculate population distributions, configurational entropy contributions, and ensemble free energies (see Experimental section for equations and methodology). This analysis compares our ovalene-like model, where both 16,7 neutral and [16,6]$^-$ anion exist as ensembles of four configurations, with the previously reported 16,6 structure, which has only one neutral configuration and two anion forms. However, one of these older anion forms is thermodynamically more favorable, determining the thermodynamic properties of the ensemble.

Table 3 presents the ensemble analysis results for the ovalene-like model, focusing on quasi-harmonic vibrational entropy treatment (qh for gas-phase and qh-tr for solution-phase calculations) for consistency with earlier calculations.[36,46,47] The methodological differences between M06-2X and RI-MP2 dramatically affect predicted population distributions. At the M06-2X level, configurations are distributed more evenly across multiple states. For [16,6]$^-$ in fluorobenzene, the most stable configuration (2O4) comprises only 40.2% of the population, with significant contributions from O3 (28%), O4a (18%), and O4b (14%). This diversity in accessible configurations yields a configurational entropy of 10.9 J K^{-1} mol^{-1} and 2.3 kJ mol^{-1} stabilization.

Table 3 Relative populations (p_i) of different configurations based on quasi-harmonic (qh) free energies, configurational entropy values (S_{conf} in J K^{-1} mol^{-1}), and the resulting stabilization of ensemble free energies (ΔG_{ens} in kJ mol^{-1}) for the most stable 16,7 neutral and [16,6]$^-$ anion structures in gas phase and fluorobenzene solution

	M06-2X			RI-MP2		
Gas-phase	p_i (qh)	S_{conf} (qh)	ΔG_{ens} (qh)	p_i (qh)	S_{conf} (qh)	ΔG_{ens} (qh)
16,7 α O3	0.00	0.9	−0.1	0.10	2.7	−0.3
16,7 α O4a	0.98			0.90		
16,7 α O4b	0.00			0.00		
16,7 α 2O4	0.02			0.00		
[16,6]$^-$ α O3	0.56	9.0	−1.4	1.00	0.0	0.0
[16,6]$^-$ α O4a	0.03			0.00		
[16,6]$^-$ α O4b	0.23			0.00		
[16,6]$^-$ α 2O4	0.18			0.00		
PhF	p_i (qh)	S_{conf} (qh)	ΔG_{ens} (qh)	p_i (qh)	S_{conf} (qh)	ΔG_{ens} (qh)
16,7 α O3	0.00	2.9	−0.3	0.68	5.2	−0.9
16,7 α O4a	0.89			0.32		
16,7 α O4b	0.00			0.00		
16,7 α 2O4	0.10			0.00		
[16,6]$^-$ α O3	0.28	10.9	−2.3	1.00	0.1	0.0
[16,6]$^-$ α O4a	0.18			0.00		
[16,6]$^-$ α O4b	0.14			0.00		
[16,6]$^-$ α 2O4	0.40			0.00		

However, at the more reliable RI-MP2 level, O3 configurations dominate overwhelmingly (> 99% for $[16,6]^-$), producing negligible configurational entropy contributions (approximately 0.1 J K^{-1} mol^{-1}). The 16,7 neutral shows greater flexibility (68% O3 in solution), generating a modest entropy of 5.2 J K^{-1} mol^{-1} and 0.9 kJ mol^{-1} stabilization.

Critically, even the largest configurational entropy contribution (2.3 kJ mol^{-1}) is negligible compared to the 51.7 kJ mol^{-1} stability advantage of our ovalene-like $[16,6]^-$ anion over the previous model. Although methodological differences yield different distribution predictions, they have no effect on our main conclusions about structural superiority. Additionally, analysis at elevated temperatures (323 K and 373 K) confirms that this configurational preference is maintained under industrially relevant polymerization conditions (see SI).

Comparison between theory and experiment

We found structural similarities between our most stable 16,7 neutral and the crystallographically characterized 26,9 sheet.[20] As illustrated in Fig. 7, our α configuration has a reactive top edge closely resembling the experimental 26,9 structure. This correspondence validates the relevance of our computational model to real MAO systems.

Additionally, we also studied $[Me_2Al(OMTS)][16,6]$ ion pair formation derived from the two lowest-energy neutral sheets: 16,7 α O3 and 16,7 α O4a. Table 4 summarizes the results from the M06-2X/TZVP level calculations in fluorobenzene PCM along with RI-MP2 energy corrections. We chose the ion pairs derived from previously reported 16,6 and crystallographically characterized 26,9 as references for stability comparison.

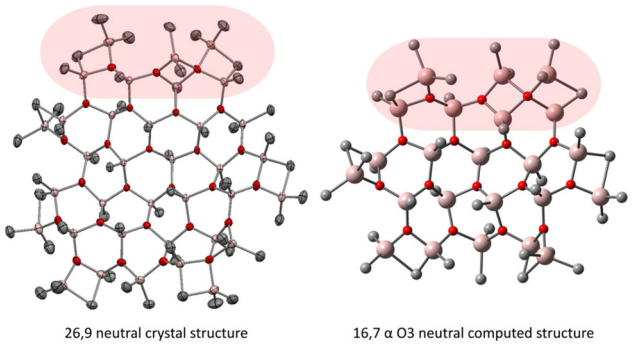

Fig. 7 Experimental structure of 26,9 with 75% probability ellipsoids depicted *vs.* our lowest energy model for 16,7.

The prevailing thermodynamic stability of the new ovalene-like $[16,6]^-$ α anions over the older model and the higher reactivity of the O3 *vs.* O4a neutrals is evident from ΔE and ΔG-qh-tr values in Table 4 (entry 1 *vs.* entries 2 and 3). The magnitude of the electronic and free energy differences (29.8 and 37.6 kJ mol^{-1}) exceeds that reported in Table 2 for the corresponding anions (21.7 and 17.5 kJ mol^{-1}). Evidently, ion-pairing, which involves both dispersive and electrostatic interactions, reveals larger differences in reactivity between these neutral sheets.

For the most stable 16,7 α neutral, formation of the most stable ion-pair (entry 3) is still somewhat less favorable than formation of the $[Me_2Al(OMTS)][26,8]$ (entry 4), even though ion-pair formation is slightly more favorable from an electronic perspective. Thus, the theoretical results indicate that if both precursors were present in similar amounts, the $[26,8]^-$ anion should be equally represented in the mass spectrum compared to $[16,6]^-$.

Since it is not (Fig. 8), this implies that either the 26,9 precursor is not present in similar amounts to that for $[16,6]^-$ or there is a large difference in sensitivity of detection for the lower *m*/*z* $[16,6]^-$ anion. We favor the former explanation, as at higher OMTS levels, the major high *m*/*z* anion is not $[26,8]^-$ but $[23,7]^-$ (Fig. 8) and given their similar *m*/*z* ratios one would not expect a marked sensitivity difference for detection of these two species.

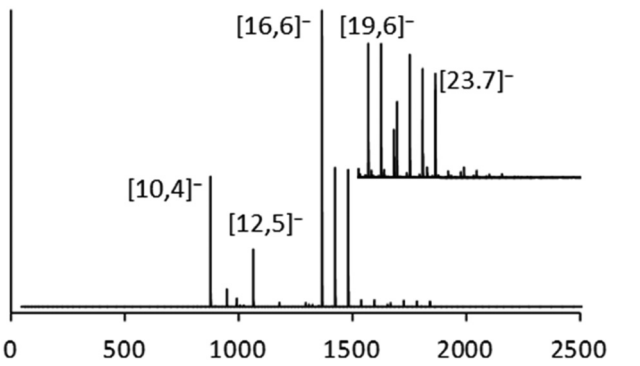

Fig. 8 Negative ion ESI-MS spectrum of commercial MAO (10 wt% W. R. Grace) and an equimolar amount of OMTS in PhF. Anion assignments are based on MS-MS experiments. The inset shows a vertical expansion of the spectrum between 1500 and 2500 Da, showing major higher *m*/*z* anions. Anions with *m*/*z* < 1300 Da are attributed to partial degradation of MAO by the large amount of OMTS present. For original spectrum see Fig. 2d in Zijlstra *et al.*, *Organometallics*, 2017.[29]

Table 4 Energetics of OMTS Ion-pair formation in fluorobenzene[a]

Entry	Reaction	ΔE	ΔG-qh-tr[c]	$\Delta\Delta E$[b]	ΔE (MP2)	ΔG-qh-tr[c] (MP2)
1	16,6 + Me_3Al-OMTS → $[Me_2Al(OMTS)][16,6]$	−67.5	4.6	−9.1	−58.4	13.7
2	16,7 α O4a + OMTS → $[Me_2Al(OMTS)][16,6$ α O4a$]$	−90.7	−22.6	−18.6	−72.1	−4.0
3	16,7 α O3 + OMTS → $[Me_2Al(OMTS)][16,6$ α O3$]$	−111.7	−51.4	−9.8	−101.9	−41.6
4	26,9 + OMTS → $[Me_2Al(OMTS)][26,8]$	−108.5	−55.9	−10.5	−98.0	−45.4

[a] Energies (kJ mol^{-1}) at 298.15 K at M06-2X/TZVP level in fluorobenzene PCM unless otherwise noted. [b] ΔE(M06-2X) − ΔE(RI-MP2) in gas phase. [c] The quasi-harmonic free energy including translational entropy corrections.

As mentioned in our previous publication, a $[26,7]^-$ anion is seen in aged MAO with OMTS,[36] and we speculated about its relationship to the 26,9 sheet isolated from a mixture of MAO and *ca.* 4.0 mol% OMTS after several months at room temperature.[20] Unfortunately, this anion appears unrelated to the $[26,8]^-$ anion that appears in both aged and unaged spectra with significantly reduced intensity. Based on its theoretical structure, the $[26,8]^-$ anion is unlikely to lose Me_3Al at low collision energies[48] and thus serve as a precursor of the $[26,7]^-$ anion through source-based, collision-induced fragmentation.[49] Evidently, further experimental work is indicated, especially now that a discrete component can be isolated from commercial material. We do note that $[16,6]^-$ is the dominant anion present at high Al : OMTS ratios (>90% of total intensity at *ca.* 100 : 1 ratios), implying that its neutral precursor is also significantly more reactive towards this donor than anything else present.

Conclusions

This work introduces a new structural model for the dominant $[16,6]^-$ anion observed in ESI-MS studies of MAO. By employing hydrocarbon–aluminoxane structural analogy rather than TMA hydrolysis pathways, we identified ovalene-like 16,7 neutral precursors that form exceptionally stable $[16,6]^-$ anions through $[Me_2Al]^+$ abstraction.

Our computational analysis reveals that structural principles derived from infinite periodic sheets require significant adaptation when applied to finite molecular systems. Edge effects and asymmetric methyl distributions fundamentally alter the optimal geometry, leading to structures that deviate from the theoretically preferred infinite sheet patterns. The most stable structure (16,7 α) produces a $[16,6]^-$ anion that is over 50 kJ mol^{-1} more stable than previously reported sheet models, finally aligning theory with experiment.

The exceptional stability arises from three synergistic factors: the ovalene-like structural framework, optimized methyl group arrangements adapted to finite molecular constraints, and enhanced preference for 3-C O environments at edge sites. The reactivity implications of these structures for metallocene-catalyzed polymerization have been explored in our companion study,[50] which demonstrates excellent agreement between calculated insertion barriers and experimental values.

These findings provide a more accurate structural foundation for understanding aluminoxane chemistry and catalyst activation mechanisms. The demonstrated importance of edge effects and finite molecular constraints has broader implications for designing and optimizing similar aluminum-based cocatalyst systems.

Experimental section

Computational studies

Geometry optimization for the infinite sheets was done in the gas phase using the M06-2X density functional[51] with specifically tailored basis sets, also used previously for periodic calculations of aluminoxanes.[17] These basis sets consisted of a standard 6-31G** basis set for hydrogen combined with the optimized 8-5-11 G* and 8-411G* basis sets for aluminum and oxygen,[52] respectively, and a 6-21G* basis set with a modified sp exponent for carbon.[53] The electronic energies were divided by 8 to obtain energies per AlOMe unit.

The finite systems were optimized using M06-2X density functional and the TZVP basis sets[54] in both the gas phase and fluorobenzene PCM.[55] Frequency calculations were performed to confirm the stationary points as minima and were also used in frequency analysis for vibrational entropy studies.

Furthermore, the M06-2X gas-phase optimized geometries were used to calculate single-point energies at the RI-MP2[56]/def2-TZVP[57] level of theory for all the finite structures. All the energy corrections employed these MP2 energies. This RI-MP2 correction method has been validated against DLPNO-CCSD(T) calculations for diverse MAO structures,[36] showing excellent agreement (typically within 1–2 kJ mol^{-1}) while maintaining computational feasibility for large systems. Gaussian 16[58] was used for all M06-2X calculations, while the RI-MP2 calculations were performed using Orca 6.0.1.[59]

Quasi-harmonic (qh) corrections to entropy and enthalpy[42] were applied using a frequency cutoff of 100 cm^{-1}. Adjustments for reduced translational entropy (tr) in solution were performed according to the procedure outlined by Whitesides and co-workers.[43] All corrections were implemented with the GoodVibes script,[60] modified to incorporate the molarity and molecular volume of fluorobenzene required for free volume calculations (PhF: 10.61 mol dm^{-3}; 120.8 $Å^3$).[36]

For the configurational ensemble thermodynamics, Boltzmann distribution was utilized to determine the relative population of each configuration (p_i):

$$p_i = \frac{e^{-\frac{G_i}{kT}}}{\sum_i e^{-\frac{G_i}{kT}}}, \quad (1)$$

where G_i is the free energy of configuration i, k is the Boltzmann constant, and T is temperature. These populations (p_i) were used to calculate the configurational entropy contribution (S_{conf}) using the Gibbs–Shannon entropy approach:[61]

$$S_{conf} = -R\sum_i p_i \ln p_i, \quad (2)$$

where R is the gas constant. The total ensemble free energy (G_{ens}) then comprises the Boltzmann-weighted contributions from individual configurations[62] plus the additional stabilization from configurational entropy:

$$G_{ens} = \sum_i p_i G_i - TS_{conf} \quad (3)$$

Author contributions

The manuscript was written through the contributions of all authors.

Conflicts of interest

There are no conflicts to declare.

Data availability

The data supporting this article have been included as part of the supplementary information (SI). Supplementary information: calculated parameters and coordinates of optimized structures. See DOI: **https://doi.org/10.1039/d5qi01957e**.

Acknowledgements

M. B. and P. H. acknowledge the support of the Research Council of Finland, decision 357509. A. V. acknowledges the financial support of the Finnish Ministry of Education and Culture through the Innovative Doctoral Education Ecosystem for Photonics I-DEEP (OKM/7/523/2024). S. C. acknowledges the University of Eastern Finland for a Visiting Scientist position. M. L. acknowledges the Academy of Finland Flagship Programme, Photonics Research and Innovation (PREIN), decision 320166. The authors acknowledge CSC – IT Center for Science, Finland, and Finnish Grid and Cloud Infrastructure (urn:nbn:fi:research-infras-2016072533) for computational resources.

References

1 H. S. Zijlstra and S. Harder, Methylalumoxane – History, Production, Properties, and Applications, *Eur. J. Inorg. Chem.*, 2015, **2015**, 19–43.
2 W. Kaminsky, Discovery of Methylaluminoxane as Cocatalyst for Olefin Polymerization, *Macromolecules*, 2012, **45**, 3289–3297.
3 F. Zaccaria, L. Sian, C. Zuccaccia and A. Macchioni, in Advances in Organometallic Chemistry, ed. P. J. Pérez, *Chapter 1: Ion pairing in transition metal catalyzed olefin polymerization*, Elsevier, San Diego, vol. 73, 2020, pp. 1–78.
4 M. Bochmann, The Chemistry of Catalyst Activation: The Case of Group 4 Polymerization Catalysts, *Organometallics*, 2010, **29**, 4711–4740.
5 F. Ghiotto, C. Pateraki, J. Tanskanen, J. R. Severn, N. Luehmann, A. Kusmin, J. Stellbrink, M. Linnolahti and M. Bochmann, Probing the Structure of Methylalumoxane (MAO) by a Combined Chemical, Spectroscopic, Neutron Scattering, and Computational Approach, *Organometallics*, 2013, **32**, 3354–3362.
6 H. Sinn, I. Schimmel, M. Ott, N. von Thienen, A. Harder, W. Hagendorf, B. Heitmann and E. Haupt, in Metalorganic Catalysts for Synthesis and Polymerization, ed. W. Kaminsky, *Chapter: Formation, structure and mechanism of oligomeric methylaluminoxanes (MAO)*, Springer Berlin Heidelberg, Berlin, Heidelberg, 1, 1999, pp. 105–122.
7 R. Tanaka, T. Kawahara, Y. Shinto, Y. Nakayama and T. Shiono, An Alternative Method for the Preparation of Trialkylaluminum-Depleted Modified Methylaluminoxane (dMMAO), *Macromolecules*, 2017, **50**, 5989–5993.
8 F. Zaccaria, P. H. M. Budzelaar, R. Cipullo, C. Zuccaccia, A. Macchioni, V. Busico and C. Ehm, Reactivity Trends of Lewis Acidic Sites in Methylaluminoxane and Some of Its Modifications, *Inorg. Chem.*, 2020, **59**, 5751–5759, and references therein.
9 S. A. Sangokoya, Method of stabilizing hydrocarbylaluminoxanes, *US Patent*, 6194340B1, 2001.
10 H. S. Zijlstra, M. C. A. Stuart and S. Harder, Structural Investigation of Methylalumoxane Using Transmission Electron Microscopy, *Macromolecules*, 2015, **48**, 5116–5119.
11 L. Luo, S. A. Sangokoya, X. Wu, S. P. Diefenbach and B. Kneale, Aluminoxane catalyst activators derived from dialkylaluminum cation precursor agents, processes for making same, and use thereof in catalysts and polymerization of olefins, *US Pat*, US8575284B2, 2013.
12 E. Y.-X. Chen and T. J. Marks, Cocatalysts for Metal-Catalyzed Olefin Polymerization: Activators, Activation Processes, and Structure–Activity Relationships, *Chem. Rev.*, 2000, **100**, 1391–1434.
13 F. Zaccaria, C. Zuccaccia, R. Cipullo, P. H. M. Budzelaar, A. Vittoria, A. Macchioni, V. Busico and C. Ehm, Methylaluminoxane's Molecular Cousin: A Well-defined and "Complete" Al-Activator for Molecular Olefin Polymerization Catalysts, *ACS Catal.*, 2021, **11**, 4464–4475.
14 T. Nakashima, Y. Nakayama, T. Shiono and R. Tanaka, Neutral, Noncoordinating, and Hydrocarbon-Soluble Protic Cocatalyst for Olefin Polymerization, *ACS Catal.*, 2021, **11**, 865–870.
15 M. E. Z. Velthoen, A. Muñoz-Murillo, A. Bouhmadi, M. Cecius, S. Diefenbach and B. M. Weckhuysen, The Multifaceted Role of Methylaluminoxane in Metallocene-Based Olefin Polymerization Catalysis, *Macromolecules*, 2018, **51**, 343–355.
16 E. Zurek and T. Ziegler, Theoretical studies of the structure and function of MAO (methylaluminoxane), *Prog. Polym. Sci.*, 2004, **29**, 107–148.
17 M. Linnolahti, J. R. Severn and T. A. Pakkanen, Are Aluminoxanes Nanotubular? Structural Evidence from a Quantum Chemical Study, *Angew. Chem., Int. Ed.*, 2006, **45**, 3331–3334.
18 S. Collins, G. Hasan, A. Joshi, J. S. McIndoe and M. Linnolahti, Are Methylaluminoxane Activators Sheets?, *ChemPhysChem*, 2021, **22**, 1326–1335.
19 A. Joshi, S. Collins, M. Linnolahti, H. S. Zijlstra, E. Liles and J. S. McIndoe, Spectroscopic Studies of Synthetic Methylaluminoxane: Structure of Methylaluminoxane Activators, *Chem. – Eur. J.*, 2021, **27**, 8753–8763.
20 L. Luo, J. M. Younker and A. V. Zabula, Structure of methylaluminoxane (MAO): Extractable $[Al(CH_3)_2]^+$ for precatalyst activation, *Science*, 2024, **384**, 1424–1428.
21 M. S. Kuklin, J. T. Hirvi, M. Bochmann and M. Linnolahti, Toward Controlling the Metallocene/Methylaluminoxane-

Catalyzed Olefin Polymerization Process by a Computational Approach, *Organometallics*, 2015, **34**, 3586–3597.

22 T. Wada and T. Taniike, Elucidation of the nano-sized molecular structure of methylaluminoxane using synchrotron X-ray total scattering, *Nanoscale*, 2025, **17**, 6767–6779.

23 K. Szeto, M. Taoufik, F. Fayon, D. Gajan, E. Zurek, J. Autschbach, J. Trébosc, L. Delevoye and R. M. Gauvin, Evidence for Methylaluminoxane (MAO) Molecular Structure and Reactivity from Ultrahigh Magnetic Field 27Al MAS NMR Spectroscopy Combined with DFT Calculations, *Angew. Chem., Int. Ed.*, 2025, **64**, e202508409.

24 M. Ystenes, J. L. Eilertsen, J. Liu, M. Ott, E. Rytter and J. A. Støvneng, Experimental and theoretical investigations of the structure of methylaluminoxane (MAO) cocatalysts for olefin polymerization, *J. Polym. Sci., Part A: Polym. Chem.*, 2000, **38**, 3106–3127.

25 E. P. Talsi, N. V. Semikolenova, V. N. Panchenko, A. P. Sobolev, D. E. Babushkin, A. A. Shubin and V. A. Zakharov, The metallocene/methylaluminoxane catalysts formation: EPR spin probe study of Lewis acidic sites of methylaluminoxane, *J. Mol. Catal. A: Chem.*, 1999, **139**, 131–137.

26 T. K. Trefz, M. A. Henderson, M. Y. Wang, S. Collins and J. S. McIndoe, Mass Spectrometric Characterization of Methylaluminoxane, *Organometallics*, 2013, **32**, 3149–3152.

27 H. S. Zijlstra, A. Joshi, M. Linnolahti, S. Collins and J. S. McIndoe, Interaction of Neutral Donors with Methylaluminoxane, *Eur. J. Inorg. Chem.*, 2019, **2019**, 2346–2355.

28 S. Collins and M. Linnolahti, Activation of Substituted Metallocene Catalysts Using Methylaluminoxane, *ChemCatChem*, 2022, **14**, e202101918, DOI: **10.1002/cctc.202101918**, and references therein.

29 H. S. Zijlstra, M. Linnolahti, S. Collins and J. S. McIndoe, Additive and Aging Effects on Methylalumoxane Oligomers, *Organometallics*, 2017, **36**, 1803–1809.

30 D. W. Imhoff, L. Simeral, D. R. Blevins and W. R. Beard, Determination of trimethylaluminum and characterization of methylaluminoxanes using proton NMR, *ACS Symp. Ser.*, 2000, **749**, 177–189.

31 R. Glaser and X. Sun, Thermochemistry of the Initial Steps of Methylaluminoxane Formation. Aluminoxanes and Cycloaluminoxanes by Methane Elimination from Dimethylaluminum Hydroxide and Its Dimeric Aggregates, *J. Am. Chem. Soc.*, 2011, **133**, 13323–13336.

32 L. Negureanu, R. W. Hall, L. G. Butler and L. A. Simeral, Methyaluminoxane (MAO) Polymerization Mechanism and Kinetic Model from Ab Initio Molecular Dynamics and Electronic Structure Calculations, *J. Am. Chem. Soc.*, 2006, **128**, 16816–16826.

33 J. T. Hirvi, M. Bochmann, J. R. Severn and M. Linnolahti, Formation of Octameric Methylaluminoxanes by Hydrolysis of Trimethylaluminum and the Mechanisms of Catalyst Activation in Single–Site α–Olefin Polymerization Catalysis, *ChemPhysChem*, 2014, **15**, 2732–2742.

34 M. Linnolahti and S. Collins, Formation, Structure, and Composition of Methylaluminoxane, *ChemPhysChem*, 2017, **18**, 3369–3374.

35 S. Collins and M. Linnolahti, Ionization of Cp_2ZrMe_2 and Lewis Bases by Methylaluminoxane: Computational Insights, *ChemPhysChem*, 2023, **24**, e202200759, DOI: **10.1002/cphc.202200759**.

36 X. Mao, M. Bharti, S. Collins and M. Linnolahti, Methylaluminoxane Reactivities and Anionic Structures: From Small Oligomers to Large Sheets, *Chem. – Eur. J.*, 2025, **31**, e202404642, DOI: **10.1002/chem.202404642**.

37 S. Collins, A. Joshi and M. Linnolahti, Formation and Structure of Hydrolytic Methylaluminoxane Activators, *Chem. – Eur. J.*, 2021, **27**, 15460–15471.

38 M. Linnolahti, A. J. Karttunen and T. A. Pakkanen, Remarkably stable icosahedral fulleranes: $C_{80}H_{80}$ and $C_{180}H_{180}$, *ChemPhysChem*, 2006, **7**, 1661–1663.

39 M. Linnolahti, T. N. P. Luhtanen and T. A. Pakkanen, Theoretical studies of aluminoxane chains, rings, cages, and nanostructures, *Chem. – Eur. J.*, 2004, **10**, 5977–5987.

40 M. Linnolahti and T. A. Pakkanen, Molecular Structures of Alumina Nanoballs and Nanotubes: A Theoretical Study, *Inorg. Chem.*, 2004, **43**, 1184–1189.

41 J. O. Sofo, A. S. Chaudhari and G. D. Barber, Graphane: A two-dimensional hydrocarbon, *Phys. Rev. B:Condens. Matter Mater. Phys.*, 2007, **75**, 153401.

42 R. F. Ribeiro, A. V. Marenich, C. J. Cramer and D. G. Truhlar, Use of Solution-Phase Vibrational Frequencies in Continuum Models for the Free Energy of Solvation, *J. Phys. Chem. B*, 2011, **115**, 14556–14562.

43 M. Mammen, E. I. Shakhnovich, J. M. Deutch and G. M. Whitesides, Estimating the Entropic Cost of Self-Assembly of Multiparticle Hydrogen-Bonded Aggregates Based on the Cyanuric Acid·Melamine Lattice, *J. Org. Chem.*, 1998, **63**, 3821–3830.

44 Using toluene as a solvent gives −50.7 kJ mol^{-1} RI-MP2 corrected free energy for $[16,6]^-$ α O3 anion compared to the reference $[16,6]^-$ anion.

45 E. V. Anslyn and D. A. Dougherty, *Modern Physical Organic Chemistry*, University Science, Sausalito, CA, 2006.

46 S. Collins and M. Linnolahti, A cooperative model for metallocene catalyst activation by methylaluminoxane, *Dalton Trans.*, 2025, **54**, 2331–2339.

47 S. Collins and M. Linnolahti, Sheet Models for Methylaluminoxane (MAO) Activators? A Theoretical Case Study involving *rac*-$Me_2Si(\eta^5\text{-}C_9H_6)_2Zr$ (SBIZr) Complexes, *ChemPhysChem*, 2024, **25**, e202300856, DOI: **10.1002/cphc.202300856**.

48 S. Collins and M. Linnolahti, Cages versus Sheets: A Critical Comparison in the Size Range Expected for Methylaluminoxane (MAO), *ChemPhysChem*, 2023, **24**, e202300342, DOI: **10.1002/cphc.202300342**.

49 A. Joshi, S. Donnecke, O. Granot, D. Shin, S. Collins, I. Paci and J. S. McIndoe, Reactive metallocene cations as sensitive indicators of gas-phase oxygen and water, *Dalton Trans.*, 2020, **49**, 7028–7036.

50 M. Bharti, A. Vähäkangas, M. Linnolahti and S. Collins, Olefin Insertion using ansa-Zirconocenes and Methylaluminoxane (MAO) involves Janus-like, Sheet Anions, *Chem. Commun.*, 2025, **61**, 18721–18724.

51 Y. Zhao and D. G. Truhlar, The M06 suite of density functionals for main group thermochemistry, thermochemical kinetics, noncovalent interactions, excited states, and transition elements: two new functionals and systematic testing of four M06-class functionals and 12 other functionals, *Theor. Chem. Acc.*, 2008, **120**, 215–241.

52 M. Catti, G. Valerio, R. Dovesi and M. Causà, Quantum-mechanical calculation of the solid-state equilibrium $MgO+\alpha\text{-}Al_2O_3 \rightleftarrows MgAl_2O_4$ (spinel) versus pressure, *Phys. Rev. B:Condens. Matter Mater. Phys.*, 1994, **49**, 14179–14187.

53 M. Catti, A. Pavese, R. Dovesi and V. R. Saunders, Static lattice and electron properties of $MgCO_3$ (magnesite) calculated by *ab initio* periodic Hartree-Fock methods, *Phys. Rev. B:Condens. Matter Mater. Phys.*, 1993, **47**, 9189–9198.

54 A. Schäfer, C. Huber and R. Ahlrichs, Fully optimized contracted Gaussian basis sets of triple zeta valence quality for atoms Li to Kr, *J. Chem. Phys.*, 1994, **100**, 5829–5835.

55 G. Scalmani and M. J. Frisch, Continuous surface charge polarizable continuum models of solvation. I. General formalism, *J. Chem. Phys.*, 2010, **132**, 114110, DOI: **10.1063/1.3359469**.

56 C. Riplinger, B. Sandhoefer, A. Hansen and F. Neese, Natural triple excitations in local coupled cluster calculations with pair natural orbitals, *J. Chem. Phys.*, 2013, **139**, 134101, DOI: **10.1063/1.4821834**.

57 F. Weigend and R. Ahlrichs, Balanced basis sets of split valence, triple zeta valence and quadruple zeta valence quality for H to Rn: Design and assessment of accuracy, *Phys. Chem. Chem. Phys.*, 2005, **7**, 3297–3305.

58 M. J. Frisch, G. W. Trucks, H. B. Schlegel, G. E. Scuseria, M. A. Robb, J. R. Cheeseman, G. Scalmani, V. Barone, G. A. Petersson, H. Nakatsuji, X. Li, M. Caricato, A. V. Marenich, J. Bloino, B. G. Janesko, R. Gomperts, B. Mennucci, H. P. Hratchian, J. V. Ortiz, A. F. Izmaylov, J. L. Sonnenberg, D. Williams-Young, F. Ding, F. Lipparini, F. Egidi, J. Goings, B. Peng, A. Petrone, T. Henderson, D. Ranasinghe, V. G. Zakrzewski, J. Gao, N. Rega, G. Zheng, W. Liang, M. Hada, M. Ehara, K. Toyota, R. Fukuda, J. Hasegawa, M. Ishida, T. Nakajima, Y. Honda, O. Kitao, H. Nakai, T. Vreven, K. Throssell, J. A. Montgomery Jr., J. E. Peralta, F. Ogliaro, M. J. Bearpark, J. J. Heyd, E. N. Brothers, K. N. Kudin, V. N. Staroverov, T. A. Keith, R. Kobayashi, J. Normand, K. Raghavachari, A. P. Rendell, J. C. Burant, S. S. Iyengar, J. Tomasi, M. Cossi, J. M. Millam, M. Klene, C. Adamo, R. Cammi, J. W. Ochterski, R. L. Martin, K. Morokuma, O. Farkas, J. B. Foresman and D. J. Fox, *GAUSSIAN 16 (Revision C.01)*, Gaussian Inc., Wallingford, CT, 2016.

59 F. Neese, Software update: The ORCA program system—Version 5.0, *Wiley Interdiscip. Rev.: Comput. Mol. Sci.*, 2022, **12**, e1606, DOI: **10.1002/wcms.1606**.

60 G. Luchini, J. V. Alegre-Requena, I. Funes-Ardoiz and R. S. Paton, GoodVibes: Automated Thermochemistry for Heterogeneous Computational Chemistry Data, *F1000Research*, 2020, **9**, 291, DOI: **10.12688/f1000research.22758.1**.

61 C. E. Shannon and W. Weaver, *The Mathematical Theory Of Communication*, The University Of Illinois Press, Urbana, 1964.

62 P. Pracht and S. Grimme, Calculation of absolute molecular entropies and heat capacities made simple, *Chem. Sci.*, 2021, **12**, 6551–6568.